

Bulk and turbulent gas motions in the interacting galaxy cluster Abell 3395 South observed with XRISM

Naomi OTA,^{1,2,*} Angie VERONICA,² Jakob DIETL,^{2,3} Anri YANAGAWA,¹ Thomas H. REIPRICH,² Veronica BIFFI,^{4,5} Klaus DOLAG,^{6,7} Marcus BRÜGGEN,⁸ Esra BULBUL,⁹ Florian PACAUD,² Yoshiki TOBA^{10,11,12}

¹Department of Physics, Nara Womens University, Kitaouyanishi-machi, Nara, Nara 630-8506, Japan

²Argelander-Institut für Astronomie (AlfA), Universität Bonn, Auf dem Hügel 71, 53121 Bonn, Germany

³Max-Planck-Institut für Radioastronomie (MPIfR), Auf dem Hügel 69, 53121 Bonn, Germany

⁴INAF – Osservatorio Astronomico di Trieste, Via Tiepolo 11, I-34143 Trieste, Italy

⁵IFPU – Institute for Fundamental Physics of the Universe, Via Beirut 2, I-34014 Trieste, Italy

⁶Universitäts-Sternwarte, Fakultüt für Physik, Ludwig-Maximilians-Universität München, Scheinerstr.1, 81679 München, Germany

⁷Max-Planck-Institut für Astrophysik, Karl-Schwarzschild-Straße 1, 85741 Garching, Germany

⁸University of Hamburg, Hamburger Sternwarte, Gojenbergsweg 112, 21029 Hamburg, Germany

⁹Max-Planck-Institut für extraterrestrische Physik, Giessenbachstraße 1, 85748 Garching, Germany

¹⁰Department of Physical Sciences, Ritsumeikan University, 1-1-1 Noji-higashi, Kusatsu, Shiga 525-8577, Japan

¹¹Academia Sinica Institute of Astronomy and Astrophysics, 11F of Astronomy-Mathematics Building, AS/NTU, No.1, Section 4, Roosevelt Road, Taipei 10617, Taiwan

¹²Research Center for Space and Cosmic Evolution, Ehime University, 2-5 Bunkyo-cho, Matsuyama, Ehime 790-8577, Japan

*E-mail: naomi@cc.nara-wu.ac.jp

ORCID: 0000-0002-2784-3652, 0000-0002-8635-0030, 0009-0001-6898-0004, 0009-0009-3388-2509, 0000-0003-2047-2884, 0000-0001-9260-3826, 0000-0003-1750-286X, 0000-0002-3369-7735, 0000-0002-7619-5399, 0000-0002-6622-4555, 0000-0002-3531-7863

Abstract

We investigate the gas motions in the core region of the Abell 3395 South subcluster (A3395S) using high-resolution X-ray spectroscopy with XRISM/Resolve. By analyzing the Fe XXV He α emission line, we directly measure the line-of-sight bulk and turbulent velocities of the intracluster medium. We find that the one-dimensional turbulent velocity is low, at the level of $124 \pm 21 \text{ km s}^{-1}$, while a significant line-of-sight bulk velocity of $263 \pm 23 \text{ km s}^{-1}$ is detected. The coexistence of low turbulence and finite bulk motion suggests that A3395S has not yet reached a dynamically relaxed state. These results are consistent with the non-detection of a radio halo in A3395S, implying that turbulent particle reacceleration is currently inefficient in the cluster core. This study demonstrates that high-resolution X-ray spectroscopy with XRISM provides a powerful means to directly constrain intracluster medium dynamics in merging galaxy clusters, and it provides a reference for future comparative studies of A3395N and A3391 within the same large-scale structure.

Keywords: galaxies: clusters: individual (A3395S) — galaxies: clusters: intracluster medium — X-rays: galaxies: clusters — galaxies: active

1 Introduction

Galaxy clusters are the most massive gravitationally bound objects in the Universe, with most of their baryonic mass residing in the intracluster medium (ICM), a hot plasma with temperatures of several keV (e.g., Böhringer & Werner (2010)). Gas motions in the ICM provide key insights into cluster assembly processes, including mergers, active galactic nucleus (AGN) feedback, and gas accretion along large-scale filaments, and they influence energy dissipation, metal transport, and non-thermal phenomena such as diffuse radio emission.

Direct measurements of ICM bulk and turbulent motions were long limited by the spectral resolution of X-ray instruments. Prior to the advent of microcalorimeter spectroscopy, constraints were obtained from emission-line measurements with CCD and grating instruments as well as from indirect methods based on surface-brightness and pressure fluctuations, although with limited preci-

sion (e.g., Ota (2012); Sanders (2023); Zhuravleva et al. (2018)). High-resolution X-ray spectroscopy now enables accurate Doppler measurements of emission-line centroids and widths. Numerical simulations have demonstrated that Fe-line shifts and broadening provide robust probes of ICM kinematics under realistic observational conditions (Dolag et al. 2005; Ota et al. 2018; Biffi et al. 2022b). This capability was first demonstrated by Hitomi in the Perseus cluster, which revealed unexpectedly low turbulent velocities in the core despite ongoing AGN activity (Hitomi Collaboration et al. 2016, 2018).

The X-ray Imaging and Spectroscopy Mission (XRISM; Tashiro et al. (2025)), equipped with the Resolve microcalorimeter (Ishisaki et al. 2018), enables systematic measurements of ICM gas motions in nearby clusters. Early XRISM results have revealed a wide diversity of dynamical states and highlighted tensions with numerical simulations, particularly in cluster cores where simulations tend to predict higher velocity dispersions than observed

(XRISM Collaboration et al. 2025b). These findings motivate interpreting individual XRISM measurements in the context of each cluster’s assembly history and environment.

Cosmological simulations predict that ICM dynamics depend on a cluster’s connectivity to the surrounding large-scale structure: clusters embedded in filaments are expected to exhibit enhanced bulk motions and anisotropic velocity fields driven by continuous accretion and repeated interactions, while a substantial fraction of the kinetic energy may remain in coherent motions rather than being fully dissipated into small-scale turbulence and heat (Zinger et al. 2016; Gouin et al. 2021). Observational tests of these predictions require measurements of both bulk and turbulent gas motions in well-characterized filamentary environments.

The Abell 3391–3395 system is a nearby ($z \simeq 0.05$) galaxy cluster complex embedded in a prominent large-scale filament, consisting of Abell 3395 South (A3395S), Abell 3395 North (A3395N), and Abell 3391 (A3391). Previous X-ray observations revealed disturbed morphologies and temperature structures in A3395S and A3395N (Forman et al. 1981; Markevitch et al. 1998; Tittley & Henriksen 2001; Lakhchaura et al. 2011). On larger scales, diffuse X-ray emission bridging A3391 and A3395 has been detected (Planck Collaboration et al. 2013; Sugawara et al. 2017; Alvarez et al. 2018), and Spectrum-Roentgen-Gamma (SRG)/eROSITA (Predehl et al. 2021) uncovered a ~ 15 Mpc warm-hot filament and a bridge-like X-ray structure between A3395S and A3395N (Reiprich et al. 2021; Veronica et al. 2022; Biffi et al. 2022a), establishing this system as part of the cosmic web (figure 1a). ASKAP/EMU observations further show that A3395S hosts a central FR I radio galaxy but no diffuse radio halo or bridge emission (Brüggen et al. 2021), providing additional constraints on turbulence and particle acceleration.

In this paper, we present XRISM/Resolve observations of A3395S and directly measure the line-of-sight bulk and turbulent velocities of the ICM from the Fe XXV He α line. We assess the dynamical state of the A3395S core in the interacting A3395S–A3395N system and compare the ICM redshift with optical galaxy redshifts to test whether the ICM is dynamically relaxed or retains signatures of ongoing interaction.

This paper is organized as follows: Section 2 describes the observations and data reduction. Section 3 presents the spectral analysis and results. In Section 4 we discuss implications for AGN feedback, merger geometry, and comparisons with numerical simulations. Section 5 summarizes our conclusions. Throughout this paper, we adopt a flat Λ CDM cosmology with $\Omega_{m0} = 0.3$, $\Omega_{\Lambda} = 0.7$, and $h = 0.7$. At $z = 0.0525$, 1' corresponds to 61 kpc. All redshifts and velocities are corrected to the Solar System barycenter, and elemental abundances are given relative to the proto-solar values of Lodders & Palme (2009).

2 Observations and data reduction

2.1 XRISM observation

Abell 3395 South (hereafter A3395S) was observed with XRISM as part of Announcement of Opportunity 1 (AO1). The observation was carried out using both the Resolve microcalorimeter (Ishisaki et al. 2018) and the Xtend X-ray imaging spectrometer (Noda et al. 2025; Uchida et al. 2025). Resolve provides high energy resolution required for precise measurements of emission-line centroids and widths from the ICM, while Xtend offers complementary imaging information over a wider field of view.

The XRISM observation of A3395S was performed as a sin-

gle pointing, with the cluster center placed near the center of the Resolve field of view. Details of the observation, including the observation ID, date, and total exposure time, are summarized in table 1. In this paper, measurements of gas velocities are based on the Resolve data, while Xtend data are used to assess background components. Figure 1a shows the eROSITA X-ray image of A3395S with the Resolve field of view overlaid as a green box.

2.2 Data processing and screening

Data processing and analysis were performed using the standard XRISM pipeline implemented in HEASoft 6.36, together with the XRISM calibration database version 12 (20250915). Event files were reprocessed following the standard screening criteria (The XRISM Data Reduction Guide). Inspection of the light curve confirmed that the count rate was stable throughout the observation, with no significant temporal variations. Only high-primary grade Resolve events were used for the spectral analysis.

High-resolution Resolve event data were used for the spectral analysis. The non-X-ray background (NXB) was estimated following the XRISM Resolve NXB database procedure described in the XRISM analysis documentation¹. NXB spectra were extracted from the dedicated NXB database corresponding to the observation conditions. The extracted NXB spectra were fitted with the standard NXB spectral model, and the best-fit model was used to determine the NXB normalization applied in the subsequent spectral analysis.

The cosmic X-ray background (CXB) was modeled using Xtend data, following the spectral components summarized in table 3 of Veronica et al. (2024). The CXB model consists of two Galactic thermal components described by apec models and an extragalactic power-law component. CXB spectra were extracted from circular regions located in the outer part of the Xtend field of view, outside the R_{500} radii of both A3395S and A3395N, where contamination from cluster emission is negligible. The extraction regions were centered at (RA, Dec) = (96.73905, -55.0057) with radius of 4.5 arcmin. The spectra were fitted assuming a spatially uniform surface brightness, using ancillary response files generated for a uniform sky. During the CXB fitting, the Xtend NXB was included as a fixed template model provided by the XRISM team². The best-fit normalizations of the CXB components were then rescaled according to the solid angle of the Resolve field of view and included as an additional background component in the Resolve spectral analysis. In the Resolve fits, all CXB model parameters were kept fixed to the values determined from the Xtend analysis.

The energy scale and spectral resolution of Resolve were assessed based on the publicly available gain report³. According to this report, pixel 1 and pixel 16 exhibit slightly degraded energy resolution compared to the other pixels, with full width at half maximum values of approximately 5 eV. To evaluate the impact of these pixels on the spectral analysis, we performed fits both including and excluding pixel 1 and pixel 16. We confirmed that the derived temperatures, redshifts, bulk velocities, and turbulent velocities are consistent within statistical uncertainties. In the following analysis, we use all science pixels except pixel 27 and the calibration pixel (shown in white in figure 1(b)).

¹ https://heasarc.gsfc.nasa.gov/docs/xrism/analysis/nxb/resolve_nxb_db.html

² https://heasarc.gsfc.nasa.gov/docs/xrism/analysis/nxb/nxb_spectral_models.html

³ https://heasarc.gsfc.nasa.gov/FTP/xrism/postlaunch/gainreports/2/201020010_resolve_energy_scale_report.pdf

Table 1. Observation Log for A3395S

Object	OBSID	Coordinates ^a	DATE	Exposure ^b	Fe XXV He α ^c	Fe XXVI Ly α ^c
Abell3395_South	201020010	96.7024, -54.546	2025-02-03	266.4	224	28

^a Pointing coordinates. ^b Net exposure time after data screening in kilo seconds. ^c Iron line counts without continuum component.

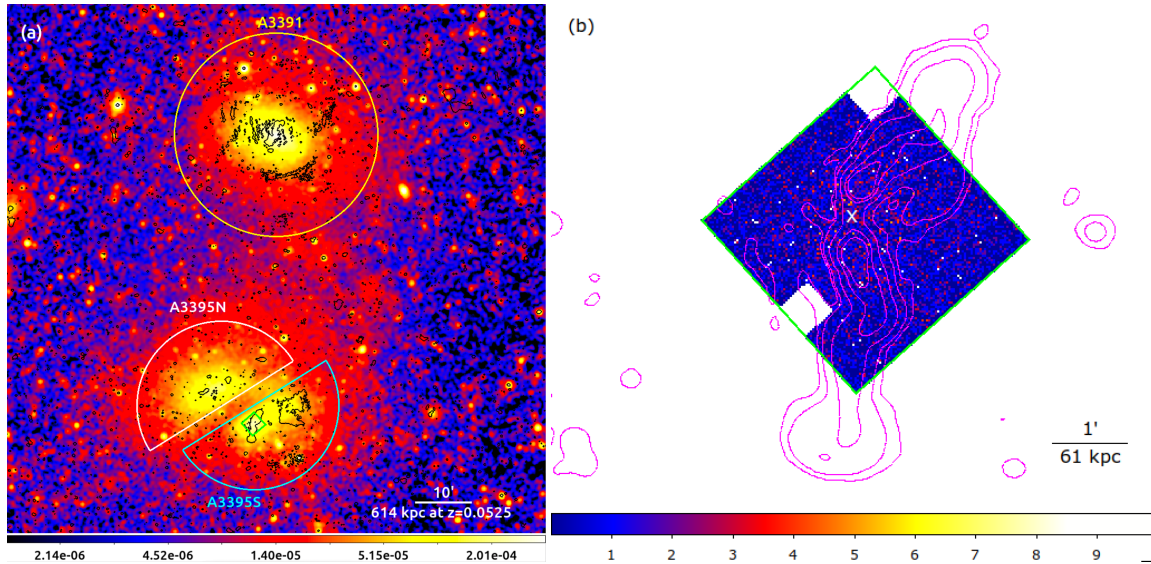


Fig. 1. (a) eROSITA X-ray image of the Abell 3391/95 system in the 0.3–2.0 keV band, particle background-subtracted, corrected for Galactic absorption, exposure-corrected, and smoothed with a 32'' Gaussian kernel. The XRISM/Resolve field of view is overlaid as a green box. A single ASKAP/EMU radio contour at $0.0001 \text{ Jy beam}^{-1}$ is shown in black (Brüggen et al. 2021). Some of the radio structure around A3391 is due to imaging artefacts. The regions used for the optical galaxy redshift analysis in Section 2.3 are indicated: a yellow circle for A3391, and white and cyan semicircles for A3395N and A3395S, respectively. (b) XRISM/Resolve X-ray image of A3395S, with the same field of view outlined in green and ASKAP/EMU radio contours overlaid. The position of the brightest cluster galaxy (BCG) is marked with a cross. The radio contour levels in panel (b) are 0.0001, 0.001, 0.01, 0.01, 0.05, and 0.1 Jy beam^{-1} . Alt text: Two-panel X-ray images illustrating the large-scale environment and the central region of the Abell 3391/95 system. Panel (a) shows the three clusters and the intercluster regions. Panel (b) focuses on the southern subcluster A3395S, where radio emission associated with the central radio galaxy traces extended jet structures.

Spectra were extracted from a region centered on the cluster core. The Resolve field of view corresponds to a radius of about $1'.5$, that is $\sim 0.065 R_{500}$ for A3395S ($R_{500} = 22'.94 = 1.39 \text{ Mpc}$; Reiprich et al. (2021)), and thus primarily probes the central core region of the cluster. XRISM measurements are dominated by the dense core emission, but remain projected quantities, implying an intrinsic uncertainty related to line-of-sight integration. Possible contamination from point sources was assessed using existing high-angular-resolution X-ray observations and was found to be negligible. The Resolve detector response matrices (RMFs) were generated using the standard XRISM tools. The ancillary response files (ARFs) were constructed assuming an extended source, using a Chandra image within a circular region of radius $3'$ as input.

Spectral fitting was performed using an absorbed thermal plasma model, $\text{tbabs} \times \text{baptec}$ (Smith et al. 2001; Foster et al. 2012). The Galactic hydrogen column density was fixed at $7.8 \times 10^{20} \text{ cm}^{-2}$ (HI4PI Collaboration et al. 2016). The NXB and CXB components described above were included as background models in the spectral fitting. Spectral fitting and error estimation were performed using the C-statistic on unbinned Resolve spectra. All spectral analyses were carried out with XSPEC version 12.15.1 (Arnaud 1996), adopting AtomDB version 3.1.3. We also verified that binning the spectra to ensure at least one count per bin yields consistent results within the statistical uncertainties.

2.3 Optical data and galaxy redshifts

Optical spectroscopic redshift information was used to characterize the galaxy component of the Abell 3391–3395 system and to provide a reference for comparison with the ICM redshift measured by XRISM. Heliocentric galaxy redshifts were collected from the NASA/IPAC Extragalactic Database (NED), selecting galaxies located in the vicinity of A3395S, A3395N, and A3391.

The A3395 system consists of two closely separated components, A3395 South (A3395S) and A3395 North (A3395N), which are close both in projected position and in redshift space. To associate galaxies with each component, we applied spatial selection criteria based on cluster-centric apertures chosen to represent each subcluster and examined the resulting redshift distributions. Because the derived mean redshifts depend on the adopted galaxy selection, the scatter among results obtained with different selection methods is treated as an estimate of the systematic uncertainty. The regions used for the optical galaxy redshift analysis are indicated in figure 1.

For A3391, the mean cluster redshift was evaluated using only galaxies located within R_{500} . This choice was made to minimize contamination from galaxies in the bridge region between A3391 and A3395, which tend to have systematically lower redshifts and can bias the cluster mean when galaxies at larger radii are included.

Brightest cluster galaxies (BCGs) were identified by visual inspection using optical images from the DESI Legacy Imaging Surveys, overlaid with X-ray surface-brightness contours from

eROSITA⁴(Kluge et al. 2024). For each cluster component, the brightest galaxy located near the X-ray peak was selected as the BCG candidate. The BCG redshifts were used as representative values for the galaxy component and compared with the ICM redshift derived from XRISM/Resolve spectroscopy. The resulting galaxy redshift distributions for A3395S, A3395N, and A3391 are shown in figure 2. The corresponding median redshifts, standard errors, and BCG redshifts for each component are summarized in table 2.

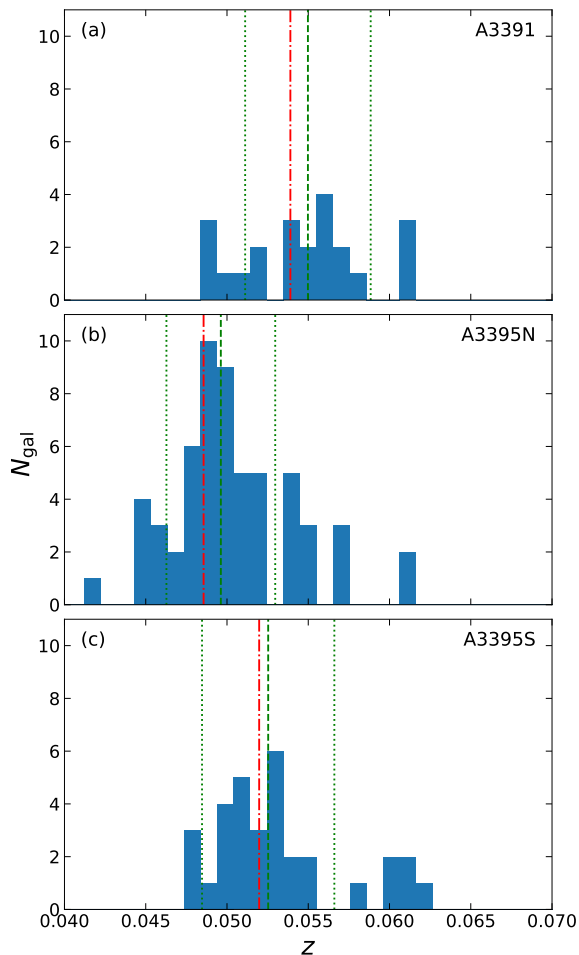


Fig. 2. Redshift distributions of galaxies associated with (a) A3391, (b) A3395N, and (c) A3395S, compiled from NED. The dot-dashed vertical lines indicate the redshifts of the brightest cluster galaxies (BCGs), while the dashed and dotted vertical lines show the median redshift of each cluster and its standard deviation, respectively. All text: Three panels showing galaxy redshift distributions for A3391, A3395N, and A3395S. Each panel displays a distinct redshift peak corresponding to the associated cluster, with differing widths that reflect variations in the galaxy velocity dispersion among the three systems.

The optical redshift information derived here is used in section 3 to quantify the line-of-sight bulk velocity of the ICM relative to the galaxy component and to assess the dynamical state of the A3395S–A3395N system.

Table 2. Optical spectroscopic redshifts

Component	$N_{\text{gal}}^{\text{a}}$	$\langle z \rangle^{\text{b}}$	σ_z^{b}	z_{BCG}
A3391	22	0.0550	0.0008	0.0539
A3395N	56	0.0496	0.0004	0.04856
A3395S	32	0.0525	0.0007	0.05198

^a Number of galaxies used to derive the cluster redshift. ^b Median spectroscopic redshift of cluster member galaxies and its standard error.

3 Analysis and results

3.1 Spectral analysis

The Resolve spectrum of A3395S clearly reveals narrow Fe XXV He α and Fe XXVI Ly α emission lines (Figure 3). Here we quote the rest-frame energies of the strongest transitions, namely Fe XXV He α w and Fe XXVI Ly α_1 , as 6.7004 and 6.9732 keV, respectively, based on AtomDB version 3.1.3 (Foster et al. 2012). As summarized in table 1, 224 and 28 counts are detected in the Fe XXV He α and Fe XXVI Ly α lines, respectively.

Spectral analysis was performed using the high-resolution Resolve data. Spectra were extracted from the entire Resolve field of view, excluding pixel 27. The spectral fitting was carried out in the 2–10 keV energy band. This band includes the Fe XXV He α and Fe XXVI Ly α emission lines, which provide the primary constraints on the temperature, redshift, and velocity broadening of the ICM. The wide energy range was adopted to simultaneously constrain the thermal continuum and the Fe line complex. The impact of restricting the fit to the Fe line band is discussed in section 3.2.

The Resolve spectra were corrected for the barycentric motion of the spacecraft relative to the Solar System barycenter. For the XRISM observation of A3395S, this corresponds to a velocity shift of approximately -3 km s^{-1} at the time of the observation. This correction was applied to ensure accurate measurements of the ICM redshift and line-of-sight bulk velocity, and its magnitude is negligible compared to the statistical uncertainties.

Figure 3 presents the Resolve spectrum and the best-fit model, while the resulting parameters are listed in table 3. The good agreement between the data and the single-temperature model indicates that the measured line widths are not dominated by unresolved multi-temperature structure along the line of sight, and are therefore likely to primarily reflect intrinsic gas motions. Although the Resolve extraction region does not exactly match those adopted in previous studies, the ICM temperature and metal abundance measured in the central region of A3395S are consistent with earlier XMM-Newton and Chandra results (e.g., Lakhchaura et al. (2011)), within the uncertainties.

3.2 Systematic uncertainties

We investigated several potential sources of systematic uncertainty that could affect the measurements of the line-of-sight bulk and turbulent velocities.

First, we examined the effect of resonant scattering by excluding the He-like Fe resonance line (the w line) from the spectral fitting. The derived bulk and turbulent velocities remained consistent within the 1σ statistical uncertainties, indicating that resonant scattering does not significantly affect our results.

Second, we tested the dependence on the adopted energy band. In addition to the baseline fit in the 2–10 keV band, we performed spectral fits restricted to the Fe-line band (5.5–7.0 keV). Although the statistical uncertainties increased due to the reduced bandpass, the best-fit velocities were consistent with those obtained from the

⁴ <https://erass-cluster-inspector.com/>

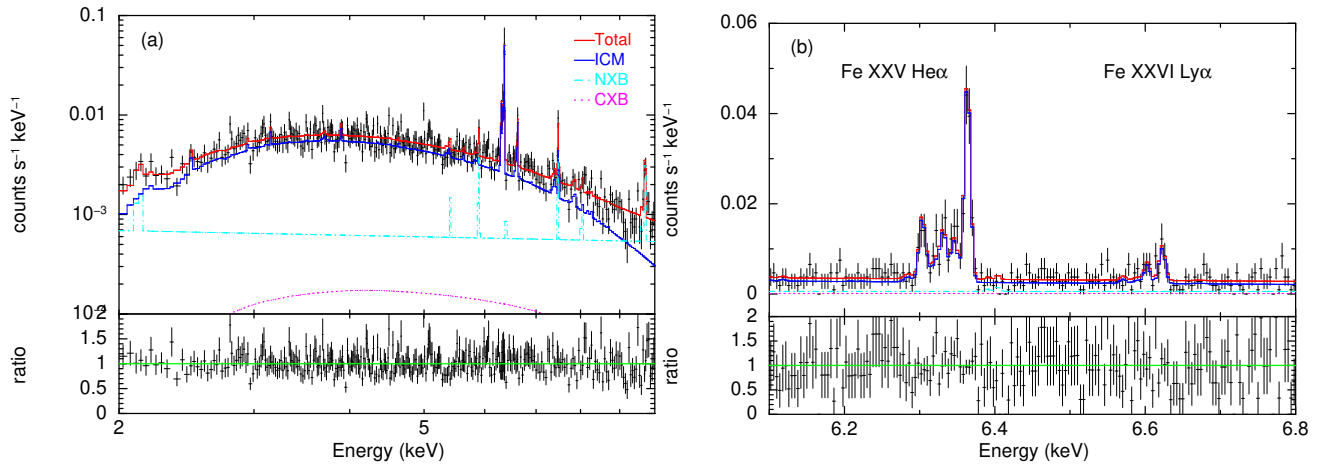


Fig. 3. (a) Resolve spectrum of A3395S in the 2–10 keV band fitted with the `bapec` model. (b) Zoom-in of the Fe XXV He α and Fe XXVI Ly α line complex. The black crosses represent the data points. In panel (a), the spectrum is grouped to achieve a statistical significance of 5σ per bin for display purposes. In panel (b), the spectrum is grouped to a fixed bin width, with one bin consisting of eight original channels (4 eV per channel). The red solid line shows the total best-fit model, while the blue solid, cyan dashed, and magenta dotted curves indicate the ICM emission, the non-X-ray background (NXB), and the cosmic X-ray background (CXB) components, respectively. Alt text: Two-panel X-ray spectra of A3395S. Panel (a) presents the overall spectral shape in the hard X-ray band, while panel (b) focuses on the iron emission line complex, illustrating the detailed line structure used to constrain the kinematic properties of the intracluster medium.

Table 3. BAPEC model fitting results

Region	kT (keV)	Z (solar)	Redshift	v_{bulk} (km s^{-1})	σ_v (km s^{-1})	norm (10^{-3}cm^{-5})	C-stat/d.o.f.	$\chi^2/\text{d.o.f.}$
Full FOV	$4.96^{+0.18}_{-0.17}$	$0.367^{+0.029}_{-0.027}$	$0.05291^{+0.00006}_{-0.00006}$	264^{+22}_{-23}	124^{+20}_{-21}	$7.65^{+0.24}_{-0.24}$	14634/15994	311/301

The uncertainties on the bulk velocity and turbulent velocity include systematic errors (section 3.2), while those on the other parameters represent statistical errors only. As a reference, the chi-squared value was calculated based on the best-fit result using a spectrum rebinned to contain at least 25 counts per bin.

full energy band.

Third, we assessed the impact of possible multi-temperature structure in the ICM by fitting the spectra with a two-temperature (`bapec+bapec`) model. The second temperature component was not statistically required, and the derived velocities were unchanged within uncertainties, suggesting that multi-temperature effects do not bias our measurements.

The systematic uncertainties associated with the Resolve energy scale and the instrumental line spread function (LSF) were evaluated using the gain recovery report for OBSID 201020010. The current 1σ systematic uncertainty of the Resolve energy scale in the 5.4–9.0 keV band is ± 0.3 eV, and the observation-specific energy offset inferred from the calibration pixel is 0.12–0.14 eV. Adding these terms in quadrature yields a total energy-scale uncertainty of ~ 0.32 – 0.33 eV, corresponding to a systematic uncertainty in the line-of-sight bulk velocity of ~ 15 km s^{-1} at 6 keV. In addition, the systematic uncertainty in the instrumental LSF is energy dependent and amounts to approximately 0.13 eV (FWHM) at 6 keV, which translates to an equivalent Gaussian width of $\sigma_E \simeq 0.055$ eV and a systematic uncertainty in the one-dimensional turbulent velocity of $\sigma_{\text{turb,sys}} \sim 3$ km s^{-1} . Both contributions are small compared to the statistical uncertainties of the measured bulk and turbulent velocities and therefore do not affect our conclusions.

Finally, we examined the impact of background modeling. The cosmic X-ray background (CXB) component is significantly smaller than the non-X-ray background (NXB) in the analyzed region. We confirmed that even allowing for a conservative $\pm 50\%$ uncertainty in the CXB normalization does not affect the best-fit

velocities, owing to the small extraction region and the dominance of the source emission.

3.3 Gas kinematics and non-thermal pressure

Based on the spectral fitting results presented in section 3.1, we investigate the kinematic properties of the ICM in A3395S, focusing on the line-of-sight bulk velocity, the turbulent velocity dispersion, and the associated non-thermal pressure support.

The line-of-sight bulk velocity of the ICM was derived from the best-fit redshift obtained with the `bapec` model. We applied the barycentric correction to the measured redshift and converted the redshift difference relative to the BCG into a velocity according to $v = c(z - z_{\text{BCG}})/(1 + z_{\text{BCG}})$. Using this definition, we measure a bulk velocity of $v_{\text{bulk}} = 264^{+22}_{-23}$ km s^{-1} .

For comparison, we also computed the bulk velocity relative to the median redshift of A3395S derived from the galaxy redshift distribution. Using $z_{\text{cluster}} = 0.0525$ as the reference, we obtain $v_{\text{bulk}} = 117 \pm 23$ km s^{-1} , where the uncertainty includes statistical and systematic contributions from the X-ray measurement only. The statistical uncertainty of the optical cluster median redshift corresponds to ~ 35 km s^{-1} , which is significantly smaller than the ~ 150 km s^{-1} offset between the BCG redshift and the cluster median. Thus, the choice of optical reference dominates over the formal statistical uncertainty of the optical redshift. This value is smaller than that obtained when adopting the BCG redshift, reflecting the offset of the BCG from the cluster median; however, the qualitative conclusion that the ICM exhibits a finite line-of-sight bulk motion remains unchanged.

The line-of-sight turbulent velocity dispersion is measured to be $\sigma_v = 124_{-21}^{+20} \text{ km s}^{-1}$. Assuming isotropic turbulence, this corresponds to a three-dimensional turbulent velocity $v_{\text{turb},3\text{D}} = \sqrt{3}\sigma_v$. The turbulent Mach number is defined as $\mathcal{M}_{\text{turb}} = v_{\text{turb},3\text{D}}/c_s$, where the adiabatic sound speed is given by $c_s = \sqrt{\gamma kT/(\mu m_p)}$, with $\gamma = 5/3$ and mean molecular weight $\mu = 0.61$. Using the best-fit temperature, we obtain a turbulent Mach number of $\mathcal{M}_{\text{turb}} = 0.188_{-0.031}^{+0.030}$, indicating that the turbulent gas motions in the core of A3395S are clearly subsonic. The derived turbulent Mach number should therefore be regarded as an upper limit on the true level of turbulence, since unresolved bulk motions along the line of sight may also contribute to the measured velocity dispersion.

The non-thermal pressure associated with turbulent motions is estimated as $P_{\text{turb}} = \rho v_{\text{turb},3\text{D}}^2/3$, where ρ is the gas mass density, and the ratio of turbulent to thermal pressure is given by $P_{\text{turb}}/P_{\text{th}} = \mu m_p v_{\text{turb},3\text{D}}^2/(3kT)$. We find that the turbulent pressure contributes only a small fraction of the total pressure budget, with $P_{\text{turb}}/P_{\text{th}} = 0.020_{-0.006}^{+0.007}$.

We also estimate the non-thermal pressure by including both the bulk and turbulent velocity components as $P_{\text{nth,tot}} = \rho(v_{\text{bulk}}^2 + v_{\text{turb},3\text{D}}^2)/3$, which yields $P_{\text{nth,tot}}/P_{\text{th}} = 0.050_{-0.007}^{+0.008}$. Even when both velocity components are taken into account, the non-thermal pressure support remains modest, indicating that gas motions are dynamically subdominant in the core of A3395S and that the ICM within the Resolve field of view is close to hydrostatic equilibrium, despite the ongoing interaction on larger scales.

4 Discussion

4.1 Low turbulent velocity and comparison with the radio AGN

The high-resolution XRISM/Resolve spectroscopy reveals that the line-of-sight turbulent velocity in the core region of A3395S is as low as $\sim 120 \text{ km s}^{-1}$. This value is remarkably small for a system undergoing a merger and is comparable to that measured in the Perseus cluster core (Hitomi Collaboration et al. 2016, 2018; XRISM Collaboration et al. 2025c), where weak turbulence was found despite the presence of a central radio AGN. Such low turbulent velocities may reflect either a relatively large effective viscosity in the intracluster medium (ICM), leading to dissipation on large spatial scales, or a situation in which merger-driven motions have not yet cascaded to smaller scales.

A3395S hosts a central FR I radio galaxy, S1 (PKS 0625–545), associated with the brightest cluster galaxy (Brüggen et al. 2021). ASKAP observations show that its jets and lobes extend over several hundred kiloparsecs ($\sim 6'$, corresponding to $\sim 370 \text{ kpc}$). Chandra data indicate that the radio structures are located near regions of steep ICM surface-brightness gradients, suggesting interaction with the surrounding gas; however, there is no clear evidence for prominent X-ray cavities or strong shocks, implying relatively gentle AGN feedback at present.

Although turbulence confined to a very small central region cannot be ruled out given the limited spatial resolution of XRISM, the absence of clear X-ray cavities and the field-of-view-averaged measurement ($3' \times 3'$) indicate that strong, volume-filling turbulence is not currently present in the core. Localized AGN-driven motions may exist but would be strongly diluted in the emission-weighted spectrum. In this respect, A3395S may represent an earlier evolutionary phase than systems such as M87, where XRISM has resolved enhanced velocity dispersion associated with mature

AGN-driven cavities (XRISM Collaboration et al. 2025a).

No diffuse radio halo has been detected in A3395S, although a triangular-shaped diffuse radio feature west of the cluster has been suggested to be a radio relic or re-accelerated plasma related to a radio AGN (Reiprich et al. 2021; Brüggen et al. 2021). Since radio halos are commonly interpreted as signatures of turbulent re-acceleration during mergers, their absence is consistent with the low level of turbulence inferred from XRISM and supports the view that large-scale turbulent motions have not yet fully developed. While this does not exclude past merger activity, it suggests that A3395S and A3395N have not reached a post-merger phase characterized by well-developed, volume-filling turbulence.

Cosmological simulations further suggest that turbulence in merging clusters can be spatially intermittent rather than volume-filling, which would reduce the velocity dispersion inferred from line broadening when averaged over the bright core (Vazza & Brunetti 2026). This effect should be considered when interpreting the low turbulent velocity measured in A3395S.

4.2 Bulk velocity and merger geometry

The XRISM/Resolve spectroscopy reveals a significant line-of-sight bulk velocity of the ICM in the core of A3395S, indicating that the hot gas is not at rest with respect to the cluster systemic redshift and that the system is dynamically unrelaxed. This interpretation is supported by optical measurements showing a redshift offset between the galaxy populations of A3395S and A3395N, as well as by the disturbed X-ray morphology and the presence of an X-ray-emitting bridge connecting the two subclusters. Previous studies have also reported an offset between the brightest cluster galaxy and the X-ray centroid in A3395S (Brüggen et al. 2021), further supporting a disturbed dynamical state.

The measured bulk velocity represents only the line-of-sight component of the three-dimensional gas motion; the true relative velocity between the interacting subclusters may therefore be larger. A substantial fraction of the merger-driven motion could lie in the plane of the sky. We searched for spatial variations in the bulk velocity by dividing the Resolve field of view into two subregions. Although the best-fit velocities differ, the statistical significance of the difference is low given the limited photon statistics and PSF mixing, and no robust velocity gradient can be established.

On larger scales, the median redshifts of A3395S and A3395N differ by $\Delta z \simeq 0.0029$ (table 2), corresponding to a line-of-sight velocity difference of $\Delta v_{\text{los}} \simeq 830 \pm 40 \text{ km s}^{-1}$. Together with the X-ray-emitting band between A3395S and A3395S (Reiprich et al. 2021), this suggests that the ongoing interaction has a significant line-of-sight component. In such a configuration, the intracluster gas may lag behind the collisionless galaxy and dark matter components, as expected in merging systems with a non-negligible line-of-sight merger geometry.

The combination of a finite bulk velocity and a low turbulent velocity provides an important constraint on the dynamical state of the core. Following Zhuravleva et al. (2012), the ratio between the line-of-sight bulk velocity and the turbulent velocity dispersion, $u_{\text{los}}/\sigma_{\text{los}}$, serves as an indicator of the dominant spatial scale of gas motions. For the full Resolve field of view, we obtain $u_{\text{los}}/\sigma_{\text{los}} \simeq 2$, implying that the kinetic energy in the core is dominated by coherent, large-scale motions rather than small-scale turbulence.

These results suggest that A3395S is in an early-to-intermediate merger stage, where large-scale gas motions are already present

but the turbulent cascade has not yet fully developed. Although projection effects and limited photon statistics prevent a detailed reconstruction of the three-dimensional merger geometry, the XRISM measurements demonstrate that bulk motions and turbulence can be decoupled in interacting clusters.

4.3 Comparison with numerical simulations

The coexistence of low turbulent velocity and significant bulk motion indicates that a substantial fraction of the kinetic energy in A3395S is stored in coherent large-scale flows rather than in fully developed small-scale turbulence within the cluster core.

This interpretation can be discussed in the context of cosmological hydrodynamical simulations of clusters embedded in large-scale filaments. Based on a comparison between SRG/eROSITA observations and Magnetium simulations, Biffi et al. (2022a) showed that the Abell 3391–3395 system is embedded in a prominent filamentary structure and that gas motions are strongly influenced by anisotropic accretion and infall along the intercluster axis on scales of several hundred kiloparsecs to megaparsecs. In such a configuration, substantial kinetic energy can be carried by coherent, directional flows and infalling clumps associated with the large-scale structure.

The velocity dispersion measured with XRISM is emission-weighted along the line of sight and is therefore dominated by the densest gas within the central region covered by the Resolve field of view. The observed turbulent velocity thus reflects primarily the dynamical state of the cluster core, rather than the full volume-averaged velocity field on megaparsec scales. Consequently, large-scale bulk flows associated with filamentary accretion may coexist with relatively low velocity dispersion in the dense core if the transfer of kinetic energy from large-scale motions to small-scale turbulence is inefficient or still developing.

In this sense, the low turbulent velocity measured by XRISM does not imply the absence of significant gas motions in the system as a whole. Rather, it suggests that in the current dynamical stage of A3395S, a considerable fraction of the merger- or accretion-driven kinetic energy has not yet been converted into volume-filling turbulence within the core region. A more quantitative comparison, for example through mock XRISM observations derived from simulations and analyzed with the same pipeline as the data, will be required to directly connect the emission-weighted observational constraints with the underlying three-dimensional velocity field. This will be explored in future work.

5 Summary

We have investigated the gas motions in the core region of the Abell 3395 South subcluster (A3395S) using high-resolution X-ray spectroscopy with XRISM/Resolve. By analyzing the Fe XXV He α complex, supplemented by Fe XXVI Ly α , we directly constrained the line-of-sight bulk and turbulent velocities of the intracluster medium (ICM).

We find that the one-dimensional turbulent velocity in the central region of A3395S is low, at the level of $\sim 100 \text{ km s}^{-1}$, indicating a relatively quiescent ICM despite the ongoing merger and the presence of a central radio AGN. In contrast, a significant line-of-sight bulk velocity of $\sim 260 \text{ km s}^{-1}$ is detected, suggesting that A3395S has not yet reached a dynamically relaxed state and that large-scale coherent gas motions are still present.

The low level of turbulence is consistent with the non-detection of a radio halo in A3395S, implying that turbulent reacceleration

is currently inefficient in the cluster core. This study demonstrates the capability of XRISM to directly probe ICM dynamics in merging clusters. Future comparative analyses of A3395N and A3391 will provide further insight into the roles of cluster mergers and AGN feedback in driving gas motions within large-scale structures.

References

- Alvarez, G. E., Randall, S. W., Bourdin, H., Jones, C., & Holley-Bockelmann, K. 2018, *ApJ*, 858, 1, 44
- Arnaud, K. A., in G. H. Jacoby & J. Barnes, eds., *Astronomical Data Analysis Software and Systems V* (1996), vol. 101 of *Astronomical Society of the Pacific Conference Series*, p. 17
- Biffi, V., Dolag, K., Reiprich, T. H., Veronica, A., Ramos-Ceja, M. E., Bulbul, E., Ota, N., & Ghirardini, V. 2022a, *A&A*, 661, A17
- Biffi, V., ZuHone, J. A., Mroczkowski, T., Bulbul, E., & Forman, W. 2022b, *A&A*, 663, A76
- Böhringer, H. & Werner, N. 2010, *A&AR*, 18, 1-2, 127
- Brüggen, M. et al. 2021, *A&A*, 647, A3
- Dolag, K., Vazza, F., Brunetti, G., & Tormen, G. 2005, *MNRAS*, 364, 3, 753
- Forman, W., Bechtold, J., Blair, W., Giacconi, R., van Speybroeck, L., & Jones, C. 1981, *ApJL*, 243, L133
- Foster, A. R., Ji, L., Smith, R. K., & Brickhouse, N. S. 2012, *ApJ*, 756, 128
- Gouin, C., Bonnaire, T., & Aghanim, N. 2021, *A&A*, 651, A56
- HI4PI Collaboration et al. 2016, *A&A*, 594, A116
- Hitomi Collaboration et al. 2016, *Nature*, 535, 7610, 117
- Hitomi Collaboration et al. 2018, *PASJ*, 70, 2, 9
- Ishisaki, Y. et al. 2018, *Journal of Low Temperature Physics*, 193, 5-6, 991
- Kluge, M. et al. 2024, *A&A*, 688, A210
- Lakhchaura, K., Singh, K. P., Saikia, D. J., & Hunstead, R. W. 2011, *ApJ*, 743, 1, 78
- Lodders, K. & Palme, H. 2009, *Meteoritics and Planetary Science Supplement*, 72, 5154
- Markevitch, M., Forman, W. R., Sarazin, C. L., & Vikhlinin, A. 1998, *ApJ*, 503, 1, 77
- Noda, H. et al. 2025, *PASJ*, 77, S10
- Ota, N. 2012, *Research in Astronomy and Astrophysics*, 12, 8, 973
- Ota, N., Nagai, D., & Lau, E. T. 2018, *PASJ*, 70, 3, 51
- Planck Collaboration et al. 2013, *A&A*, 550, A134
- Predehl, P. et al. 2021, *A&A*, 647, A1
- Reiprich, T. H. et al. 2021, *A&A*, 647, A2
- Sanders, J. S., in C. Bambi & J. Jiang, eds., *High-Resolution X-ray Spectroscopy: Instrumentation* (2023), pp. 173–207
- Smith, R. K., Brickhouse, N. S., Liedahl, D. A., & Raymond, J. C. 2001, *ApJL*, 556, L91
- Sugawara, Y., Takizawa, M., Itahana, M., Akamatsu, H., Fujita, Y., Ohashi, T., & Ishisaki, Y. 2017, *PASJ*, 69, 6, 93
- Tashiro, M. et al. 2025, *PASJ*, 77, S1
- Tittley, E. R. & Henriksen, M. 2001, *ApJ*, 563, 2, 673
- Uchida, H. et al. 2025, *PASJ*, 77, S23
- Vazza, F. & Brunetti, G. 2026, *A&A*, 705, A129
- Veronica, A. et al. 2022, *A&A*, 661, A46
- Veronica, A. et al. 2024, *A&A*, 681, A108
- XRISM Collaboration et al. 2025a, arXiv e-prints, arXiv:2512.06596
- XRISM Collaboration et al. 2025b, *ApJL*, 993, 1, L11
- XRISM Collaboration et al. 2025c, arXiv e-prints, arXiv:2509.04421
- Zhuravleva, I., Allen, S. W., Mantz, A., & Werner, N. 2018, *ApJ*, 865, 1, 53
- Zhuravleva, I., Churazov, E., Kravtsov, A., & Sunyaev, R. 2012, *MNRAS*, 422, 3, 2712
- Zinger, E., Dekel, A., Birboim, Y., Kravtsov, A., & Nagai, D. 2016, *MNRAS*, 461, 1, 412

Acknowledgments

We thank the XRISM project and the mission operations team for the operation of the satellite and their support of the observations. This work was supported by JSPS KAKENHI Grant Number 25K01026, 23H00121 (NO). This work was also supported by the Humboldt Japan–Germany Fellowship for Joint Research (NO, AV). NO acknowledges partial support by the Organization for the Promotion of Gender Equality at Nara Women’s University. AY acknowledges support by JST SPRING, Grant Number JPMJSP2115. MB acknowledges funding by the Deutsche Forschungsgemeinschaft (DFG) under Germany’s Excellence Strategy – EXC 2121 “Quantum Universe” – 390833306 and the DFG Research Group “Relativistic Jets”. This research has made use of the NASA/IPAC Extragalactic Database (NED), which is operated by the Jet Propulsion Laboratory, California Institute of Technology, under contract with the National Aeronautics and Space Administration.

This work is based on data from eROSITA, the soft X-ray instrument aboard SRG, a joint Russian–German science mission supported by the Russian Space Agency (Roskosmos), in the interests of the Russian Academy of Sciences represented by its Space Research Institute (IKI), and the Deutsches Zentrum für Luft- und Raumfahrt (DLR). The SRG spacecraft was built by Lavochkin Association (NPOL) and its subcontractors, and is operated by NPOL with support from the Max Planck Institute for Extraterrestrial Physics (MPE).

The development and construction of the eROSITA X-ray instrument was led by MPE, with contributions from the Dr. Karl Remeis Observatory Bamberg & ECAP (FAU Erlangen–Nuernberg), the University of Hamburg Observatory, the Leibniz Institute for Astrophysics Potsdam (AIP), and the Institute for Astronomy and Astrophysics of the University of Tübingen, with the support of DLR and the Max Planck Society. The Argelander Institute for Astronomy of the University of Bonn and the Ludwig Maximilians Universität Munich also participated in the science preparation for eROSITA.